
A recent decline in North Atlantic subtropical mode water formation

Stevens Samuel W. ^{1,2,*}, Johnson Rodney J. ², Maze Guillaume ³, Bates Nicholas R. ^{2,4}

¹ Earth, Ocean and Atmospheric Sciences Department, University of British Columbia, Vancouver, British Columbia, Canada

² Bermuda Institute of Ocean Sciences, St. George's, Bermuda

³ Ifremer, University of Brest, CNRS, IRD, Laboratoire d'Océanographie Physique et Spatiale (LOPS), IFREMER, Brest, France

⁴ Ocean and Earth Science Department, University of Southampton, Southampton, UK

* Corresponding author : Samuel W. Stevens, email address : sstevens@eoas.ubc.ca

Abstract :

As a manifestation of mixing dynamics in the upper ocean, interannual and decadal variability of subtropical mode water (STMW) properties in the North Atlantic Ocean provides a valuable insight into ocean–atmosphere interaction in a changing climate. Here, we use hydrographic data from the Bermuda Atlantic Time-Series Study and Hydrostation S sites near Bermuda, as well as various ocean reanalysis products, to evaluate the modern variability of STMW properties. Our study finds an 86–93% loss of STMW thickness at these sites between 2010 and 2018 and a comparable loss throughout the western subtropical gyre, culminating in the weakest STMW pentad on record. We correlate this decline with a reduction in the annual outcropping volume and northward excursions of the formation region, suggesting a gyre-wide signal of weakening STMW generation. The outcropping volume of STMW is anti-correlated with surface ocean heat content, foreshadowing future STMW loss in the face of continued warming.

The ocean has absorbed around one-third of all anthropogenic carbon dioxide emissions and has captured over 90% of the heat trapped by our climate system due to the buildup of greenhouse gases in the atmosphere^{1,2}. Investigating how oceanic water masses change over large time-scales can help us understand how the ocean sequesters heat and carbon away from the atmosphere and into the interior³. One climatologically significant water mass is Subtropical Mode Water (STMW): a vertically homogeneous water mass existing between the seasonal and permanent thermoclines of the Atlantic and Pacific subtropical gyres. In the North Atlantic, winter cooling and convection creates deep mixed layers and forms two physically similar “flavours” of STMW⁴. Thermal stratification at the surface caps these mixed layers during the spring and the

newly-formed STMW is then advected away from the formation zones, imprinting a signal of winter mixing across large regions of the subtropical North Atlantic^{5,6}.

The volume occupied by North Atlantic STMW is around 75 Svy—with 1 Svy equivalent to a flow of 1 Sv ($10^6 \text{ m}^3 \text{ s}^{-1}$) for a year ($3.15 \times 10^{13} \text{ m}^3$)—and wintertime contributions to the STMW volume budget are as large as 8.6 Svy due to convection and buoyancy loss⁷. This formation estimate is of comparable magnitude to other notable North Atlantic water masses (e.g. North Atlantic Deep Water formation of 13.0 Svy⁸), underlining STMW as an important storage and transport mechanism for properties such as heat and freshwater^{9,10}. Additionally, STMW plays an influential role in many biogeochemical processes in this region, including: (1) sequestering significant amounts of inorganic carbon from the atmosphere (20% of the overall uptake in the 14–50°N latitude band¹¹); (2) acting as a complex nutrient reservoir for photosynthetic organisms in the euphotic zone^{12,13}; and, (3) storing and exporting large magnitudes of organic carbon from the surface to the deep ocean¹⁴. As a conduit between the atmosphere and ocean interior, and an underpinning for biogeochemical processes in the subtropical gyre, STMW formation variability documents the communication and impact of climate forcing across the air-sea boundary.

Primarily due to its weak stratification, the STMW layer is well-represented as a minimum in the potential vorticity (PV) profile of the upper ocean^{15,16}. Thus, STMW PV structure and its temporal evolution are a reliable measure of its variability. During periods of weak or no renewal, destructive processes (i.e. diffusion and mixing) erode the existing STMW PV structure and properties^{17,18}. Annual renewal strength is intrinsically linked to North Atlantic Oscillation (NAO)

periodicity^{19,20}, whereby shifts in northern hemisphere atmospheric pressure can drive changes in STMW ventilation via the repositioning of storm tracks and Gulf Stream position²¹. Due to the quasi-decadal nature of the NAO²², it is vital to assess STMW properties over time-scales spanning multiple NAO cycles when attempting to resolve interannual and decadal variability.

Surface ocean stratification is strengthening in the subtropical North Atlantic due to considerable increases in heat content²³. Observations show an increase in the thermal stratification of STMW as a direct effect of surface warming²⁴ and modelling studies predict diminishing STMW formation regions in both the Pacific and Atlantic^{25,26}. It is possible that ocean warming is altering STMW formation dynamics, however neither the mechanisms, magnitude, nor impacts of these changes are fully understood. Here, we derive numerous STMW properties and climate change identifiers from observational and assimilation data products within the North Atlantic subtropical gyre and use these properties to evaluate the modern variability of STMW characteristics in a warming ocean.

Recent STMW Loss

The Bermuda Atlantic Time-series Study (BATS) and Hydrostation S studies have long been used for researching STMW variability^{21,27,28} with observations spanning from 1988 and 1954, respectively. These oceanic sites are located near Bermuda in the southern region of the STMW formation zone (Figure 1a) and represent a long-term, comprehensive dataset that is characteristic of the STMW layer throughout the entire North Atlantic subtropical gyre²⁹. Here, we use data from thou-

sands of conductivity-temperature-depth (CTD) profiles and discrete water samples collected at the BATS/Hydrostation S sites since 1955, and diverse methods to classify and document variability in STMW properties within this region.

Our study finds strong evidence for a substantial loss of North Atlantic STMW in the past decade (Figures 1c, 2, and 3, and Table 1). From 2010–2018 (all year ranges stated hereafter are inclusive), the erosional trends represent an 86–93% loss of STMW thickness, a 140–160% increase in core PV (defined here as the minima of the PV profile), and a 63–70% reduction in STMW intensity (a measure of the vertically integrated PV content within the STMW layer, see methods section for further details) since 2010. These erosional processes have accumulated over the 2010–2018 period, precipitating some of the thinnest, weakest STMW layers on record in the 2014–2018 pentad. Indeed, in 7.5% of the profiles from this pentad, there was no measurable STMW layer (STMW thickness of 0 m, Figure 2c). This loss occurred during a primarily positive NAO phase (Figure 2i), therefore a reduction in STMW formation is not unexpected. However, the unusual magnitude of deterioration during this period suggests that other mechanisms contributed to the decline in addition to NAO-associated forcing.

The physical properties of the STMW layer have also changed over the past decade. Notably, between 2010–2018, the STMW core warmed at a rate of $0.68 \pm <0.12$ °C decade⁻¹ (or 0.51–0.72 °C overall) and the STMW layer vertically integrated specific enthalpy (h_{STMW} hereafter, used as a measure of heat content, see methods section for definition) has decreased by 2112.0 ± 87.6 kJ kg⁻¹ m year⁻¹. In contrast to the STMW layer, the vertically integrated specific enthalpy of the

upper ocean (10–150 m, h_s hereafter) has increased by $97.9 \pm 11.6 \text{ kJ kg}^{-1} \text{ m year}^{-1}$. Additional physical property changes are detailed in Extended Data Figure 1.

Historical Context and the Impact of Warming

The Hydrostation S bottle dataset offers a valuable insight into STMW properties during the period predating CTD measurements (i.e. 1955–1988), allowing us to contrast STMW property trends over decadal and longer scales. Of particular interest is the signal of core PV—in this context, the PV signal largely depicts the vortex stretching component between isopycnals and is representative of the density gradient throughout the water mass (see methods for further details on PV formulation). In Figures 1c, 2e, and 3b, significant changes in the PV profile from 2010 onwards represent a more stable, stratified STMW layer. A trend of increasing thermal stratification of STMW has been observed in both the Pacific and Atlantic due to increasing ocean temperatures²⁴. This stabilisation can be seen in the PV signal presented here, signifying an erosion of one of the defining properties of STMW during recent years.

Consistent with subtropical North Atlantic trends^{30,31}, our study finds a warming in STMW core temperature of 0.42–1.26 °C per century since 1955 (see methods for more information on temperature range statistics). This is comparable to recent STMW warming estimates of 0.8–1.8 °C per century²⁴. It is notable that 2017 had the warmest STMW layer on record, with a mean core temperature of 18.97 °C, compared to 1955–2018 mean core temperature of 18.16 °C. While h_s has increased since 2010 (and as been steadily increasing since the 1990s, Figure 2h), h_{STMW}

has decreased contemporaneously in the STMW layer (Figure 2f), largely due to declining STMW thickness. These converse but related trends are both seemingly linked to surface warming; rising temperatures increase the specific enthalpy and thermal stratification of surface waters while simultaneously stabilising and eroding STMW layers. This drives an enhanced partitioning of energy throughout the upper ocean, with more energy stored near the surface and less energy sequestered into the ocean interior (Figure 3a), and has implications for the North Atlantic’s capacity to remove and store heat from a warming atmosphere.

To contextualise the magnitude of STMW loss during the 2014–2018 pentad, we compared STMW properties during this period to other weak events in the historical record. One such event occurred in the 1970s²⁸, during which weak renewal induced remarkably cold and thin STMW layers. Sensitivity analysis around this period reveals that the weakest STMW pentad occurred from 1971 to 1975 (inclusive). By most measures of thickness and core PV, the 2014–2018 event has thinner, more stratified STMW layers when compared with the 1971–1975 event (Extended Data Figure 2)—strong evidence that the 2014–2018 event represents the weakest STMW formation period on record.

We further evaluate STMW variability at the Bermuda time-series sites using a synthesis of hydrographic data from numerous reanalysis and observational sources: (1) Argo floats profiling within the STMW formation zone³²; (2) EN4g10, the Met Office Hadley Centre’s “EN” monthly objective analyses product³³; and (3) ORAS4, the European Centre for Medium-Range Weather Forecasts (ECMWF) monthly reanalysis product³⁴ (see methods for further details on additional

datasets). The signals derived from these data are consistent with the Bermuda time-series observations, inferring that there have been robust changes in STMW properties since 2010—namely, decreased STMW thickness and increased PV coupled with increasing temperatures (Figure 4).

Formation Zone Variability

Advective processes mostly drive the interannual variability in STMW volume at Bermuda and throughout the North Atlantic subtropical gyre^{9,28}. Indeed, it is rare for STMW formation to occur at the BATS/Hydrostation S sites (<19 °C isotherm outcropping indicated on Figure 2a and b), and these events are primarily restricted to generating only the warmest and shallowest content of the layer. Thus, STMW variability and erosional trends are likely indicators of changes in formation rate processes communicated to the BATS/Hydrostation S sites via advection.

To assess STMW formation variability, we used the Met Office EN4g10 1° x 1° objective analyses dataset from January 1955–July 2019 to map thickness and isopycnal changes (Figure 5), and the EN4g10 and ECMWF ORAS4 datasets to calculate the annual February-April (inclusive) STMW outcropping volume (Figure 4e; see methods for calculation and formation zone details; all statistics in this section are calculated using annual mean property values; values separated by a slash represent EN4g10 and ORAS4 estimates, respectively). Throughout the record, there is a significant correlation between outcropping volume and Bermuda STMW thickness ($r = 0.36/0.29$, p -values = <0.05). The volume of STMW formation is found to have reduced at a rate of 0.46 ± 0.29 Svy/ 0.44 ± 0.32 Svy since 2010. This trend represents a reduction in outcropping volume

of 1.5–6.8 Svy/1.0–6.1 Svy from 2010–2018, suggesting that reduced ventilation was a principal driver of the weakened STMW signal. These results reinforce the coupling between formation zone variability and STMW variability at Bermuda, and support recent modelling studies that predict a reduction in mode water formation volume driven by increasingly stratified subtropical oceans^{25,26}.

The region in which STMW formed during the 2010–2018 period may have also contributed to the diminished renewal. The state of the NAO is thought to impact Gulf Stream position³⁵ and the strength of the Atlantic Meridional Overturning Circulation³⁶ (AMOC). The northward extent of the formation zone is primarily a result of Gulf Stream position and is strongly coupled with STMW renewal strength²¹. Recently, the heating of the subtropical gyre and a weakening of the AMOC has precipitated a northward shift in the Gulf Stream^{37,38}. In our study, we used the mean northward latitude of the 18 °C sea surface temperature (SST) isotherm in the North Atlantic to represent formation zone position. Using this metric, we identify an anti-correlation between STMW outcropping volume and the formation zone position ($r = -0.52/-0.39$, $p < 0.05$), and an anti-correlation between Bermuda STMW thickness and EN4g10 formation zone position ($r = -0.51$, $p < 0.01$). Recent northward excursion of the Gulf Stream translocates the formation zone position, which is farther north during 2014–2018 than during any other period (formation zone variability displayed in Figure 1a). While there is an apparent linkage between these two processes, it is unclear whether the relationship is causal or if both processes are driven by coupled climate-ocean dynamics within the North Atlantic system.

We find that h_{STMW} is decreasing overall; however, h_s is increasing concurrently (Figure 2f

and h). A strong anti-correlation has been identified between upper ocean heat content and STMW volume⁹. This relationship is due to increased heat energy in the surface layer which thermally stabilises the surface waters of the formation zone, preconditioning the region to produce warm and thin STMW layers¹⁹. We observe a similar relationship in our study, where h_s at Bermuda from 1955–2018 anti-correlates with the outcropping volume in the formation zone ($r = -0.60/0.57$, p -value = <0.01). This anti-correlation is echoed in the EN4g10 and ORAS4 data, where h_s averaged over the entire formation region is anti-correlated with outcropping volume ($r = -0.45/0.28$, p -value = <0.05). It is therefore possible that the positive surface heat budget trend observed at BATS/Hydrostation S, and throughout the entire subtropical gyre, could further diminish STMW generation and the gyre-wide ventilation of the layer.

Due to the advected nature of STMW in the subtropical North Atlantic, the variability at the BATS/Hydrostation S sites is a reliable representation of gyre-wide variability on interannual and decadal timescales²⁹. To verify this, we assessed the spatial variability of STMW erosion using the EN4g10, ORAS4, and BATS Validation (BV) dataset. The BV dataset consists of an annual transect from 34–20°N along the 66.5°W meridian. On this transect, annual CTD stations have been conducted with one-degree spatial resolution for 15–25 years (station locations on Figure 1a and 5). These observations, in combination with regional reanalysis data, confirm that STMW erosion extends beyond the BATS/Hydrostation S region (Figure 5a–i).

The spatial distribution of STMW loss during the past decade is not uniform throughout the subtropical North Atlantic (Figure 5). The largest decline in STMW thickness occurs in the

western “bowl” of the subtropical gyre; the region that generally contains the thickest and warmest STMW layers¹⁶ (Figure 5a). The thinning of STMW layers has been precipitated by a change in the isopycnal structure, evidenced by a deepening of the STMW upper boundary (Figure 1c, 3c and Figure 5j). This vertical migration (or “heaving”) of isopycnals is consistent with changes in Ekman pumping, where climatic shifts in wind stress have increased thermocline depths in the Sargasso Sea and induced a regional accumulation of heat content³⁹. The deterioration in STMW outcropping during the past decade (Figure 1a and 4e) is indicative of reduced wintertime buoyancy removal and an overall reduction in STMW renewal^{18,40}. Thus, it is feasible that a combination of reduced ventilation and stabilisation at the upper STMW boundary has precipitated the modern decline. A formal water mass formation analysis^{41,42} would further elucidate the mechanisms of reduced STMW formation, though this is beyond the scope of this study.

Conclusions

Using various measurements of STMW strength in the North Atlantic over the past six decades, we find a significant erosion of the modern STMW layer. The erosion occurred primarily in the past decade, culminating in the weakest STMW layer on record during the 2014–2018 pentad. The modern deterioration of STMW is remarkable in a historical context and is not restricted to the primary study site, but is found to span a large spatial extent throughout the subtropical gyre. We have linked the gyre-wide STMW erosion to a reduction in STMW outcropping and changes in the isopycnal structure of the subtropical gyre. The STMW outcropping volume is anti-correlated with surface heat content at the Bermuda site and throughout the formation region, indicating that

the warming of the surface ocean is restricting water mass ventilation. We also observe a coupling between reduced STMW formation strength and recent weakening of the AMOC and associated northern excursions of the Gulf Stream.

While the modern STMW layer is strongly coupled with climatic forcing during a positive NAO oscillation, NAO forcing was not anomalously weak from 2010–2018. Despite this, the STMW layer was abnormally weak during this period, indicating a potentially increasing influence of climate change dynamics on formation processes relative to natural climatic forcing. It should be noted, however, that the emergence timescales for trends in mixed-layer processes such as STMW formation are large⁴³, and there is evidence that increases in surface stratification found in climate models⁴⁴ are not necessarily reflected in observations²³. Thus, continued study into surface ocean stratification in the formation region and the communication of stratification changes into the STMW layer is necessary to better understand the long-term impact of ocean warming upon STMW properties.

Previous studies have found that anomalously cold and vigorous formation periods can reset STMW properties to more typical characteristics and that the “storage mechanism” of properties in these phases can endure through several seasons with little or no renewal⁴⁵. As such, short stretches of energetic winters can realign STMW properties toward the climatological mean. Indeed, STMW properties have seemingly been recovering since 2018, marking a probable conclusion to the modern weak STMW period. If, however, increasing ocean temperatures and a slowdown of the AMOC are impacting STMW formation, a continuation or acceleration of these trends could exacerbate

STMW loss during weak renewal periods. This sequence of events was exemplified during the past decade: substantial renewal during a strongly negative NAO event in 2011 briefly ventilated the layer, yet the signal of this ventilation was quickly attenuated in the proceeding years, yielding significant STMW erosion (Figures 2c, e, and g).

While caution is required when evaluating modern variability in the context of the more coarsely resolved 1955–1988 dataset, the contemporary STMW layer is arguably weaker than has been recorded in the past sixty years—an observation that is supported by data from various ocean reanalysis products. Although temperature and stratification changes have been observed in the STMW core prior to 2014²⁴, this is the first indication that temperature changes have impacted water mass thickness (and therefore, volume) on interannual to decadal scales over large regions of the subtropical North Atlantic. The impact of STMW formation and volume changes upon the biogeochemical processes and storage capacity of North Atlantic STMW warrants further study, especially considering the critical role that the water mass plays in sequestering anthropogenic carbon from the atmosphere.

1. Zanna, L., Khatiwala, S., Gregory, J. M., Ison, J. & Heimbach, P. Global reconstruction of historical ocean heat storage and transport. *Proceedings of the National Academy of Sciences* **116**, 1126–1131 (2019).
2. Gruber, N. *et al.* The oceanic sink for anthropogenic co₂ from 1994 to 2007. *Science* **363**, 1193–1199 (2019).

3. Chen, X. & Tung, K.-K. Varying planetary heat sink led to global-warming slowdown and acceleration. *Science* **345**, 897–904 (2014).
4. Joyce, T. M. New perspectives on eighteen-degree water formation in the North Atlantic. *Journal of Oceanography* **68**, 45–52 (2012).
5. McCartney, M. S. The subtropical recirculation of Mode Waters. *Journal of Marine Research* **40**, 427–464 (1982).
6. Maze, G. & Marshall, J. Diagnosing the observed seasonal cycle of atlantic subtropical mode water using potential vorticity and its attendant theorems. *Journal of Physical Oceanography* **41**, 1986–1999 (2011).
7. Forget, G., Maze, G., Buckley, M. & Marshall, J. Estimated Seasonal Cycle of North Atlantic Eighteen Degree Water Volume. *Journal of Physical Oceanography* **41**, 269–286 (2011).
8. Dickson, R. & Brown, J. The production of North Atlantic Deep Water: Sources, rates, and pathways. *Journal of Geophysical Research* **99**, 12319–12341 (1994).
9. Dong, S., Hautala, S. L. & Kelly, K. A. Interannual Variations in Upper-Ocean Heat Content and Heat Transport Convergence in the Western North Atlantic. *Journal of Physical Oceanography* **37**, 2682–2697 (2007).
10. Xu, X., Rhines, P. B. & Chassignet, E. P. Temperature-Salinity Structure of the North Atlantic Circulation and Associated Heat and Freshwater Transports. *Journal of Climate* **29**, 7723–7742 (2016).

11. Bates, N. R. Multi-decadal uptake of carbon dioxide into subtropical mode water of the North Atlantic Ocean. *Biogeosciences* **9**, 2649–2659 (2012).
12. Conway, T. M., Palter, J. B. & Souza, G. F. D. Gulf Stream rings as a source of iron to the North Atlantic subtropical gyre. *Nature Geoscience* **11**, 594–598 (2018).
13. Palter, J. B., Lozier, M. S. & Barber, R. T. The effect of advection on the nutrient reservoir in the North Atlantic subtropical gyre. *Nature* **437**, 687–692 (2005).
14. Carlson, C. A. *et al.* Dissolved organic carbon export and subsequent remineralization in the mesopelagic and bathypelagic realms of the North Atlantic basin. *Deep-Sea Research Part II* **57**, 1433–1445 (2010).
15. Hanawa, K. & Talley, L. D. Mode Waters. In *Ocean Circulation and Climate*, 373–386 (Elsevier, 2001).
16. Feucher, C., Maze, G. & Mercier, H. Subtropical Mode Water and Permanent Pycnocline Properties in the World Ocean. *Journal of Geophysical Research: Oceans* **124**, 1139–1154 (2019).
17. Alfultis, M. A. & Cornillon, P. Annual and Interannual Changes in the North Atlantic STMW Layer Properties. *Journal of Physical Oceanography* **31**, 2066–2086 (2000).
18. Billheimer, S. & Talley, L. D. Near cessation of Eighteen Degree Water renewal in the western North Atlantic in the warm winter of 2011-2012. *Journal of Geophysical Research: Oceans* **118**, 6838–6853 (2013).

19. Kwon, Y.-o. & Riser, S. C. North Atlantic Subtropical Mode Water: A history of ocean-atmosphere interaction 1961-2000. *Geophysical Research Letters* **31**, 1–4 (2004).
20. Peng, G., Chassignet, E. P., Kwon, Y.-o. & Riser, S. C. Investigation of variability of the North Atlantic Subtropical Mode Water using profiling float data and numerical model output. *Ocean Modelling* **13**, 65–85 (2006).
21. Joyce, T. M., Deser, C. & Spall, M. The Relation between Decadal Variability of Subtropical Mode Water and the North Atlantic Oscillation. *Journal of Climate* **13**, 2550–2569 (2000).
22. Hurrell, J. W. Decadal Trends in the North Atlantic Oscillation: Regional Temperatures and Precipitation. *Science* **269**, 676–679 (1995).
23. Somavilla, R., González-Pola, C. & Fernández-Díaz, J. The warmer the ocean surface, the shallower the mixed layer. How much of this is true? *Journal of Geophysical Research: Oceans* **122**, 7698–7716 (2017).
24. Sugimoto, S., Hanawa, K., Watanabe, T., Suga, T. & Xie, S.-p. Enhanced warming of the subtropical mode water in the North Pacific and North Atlantic. *Nature Climate Change* **7**, 656–659 (2017).
25. Lique, C. & Thomas, M. D. Latitudinal shift of the Atlantic Meridional Overturning Circulation source regions under a warming climate. *Nature Climate Change* **8**, 1013–1021 (2018).
26. Xu, L., Xie, S.-p. & Liu, Q. Mode water ventilation and subtropical countercurrent over the North Pacific in CMIP5 simulations and future projections. *Journal of Geophysical Research* **117** (2012).

27. Worthington, L. V. The 18°C water in the Sargasso Sea. *Deep Sea Research* **5**, 297–305 (1959).
28. Talley, L. D. & Raymer, M. E. Eighteen Degree Water Variability. *Journal of Marine Research* **40**, 757–775 (1982).
29. Jenkins, W. J. On the climate of a subtropical ocean gyre: Decadal time scale variations in water mass renewal in the Sargasso Sea. *Journal of Marine Research* **40**, 265–290 (1982).
30. Deser, C., Phillips, A. S. & Alexander, M. A. Twentieth century tropical sea surface temperature trends revisited. *Geophysical Research Letters* **37**, 1–6 (2010).
31. Wu, L. *et al.* Enhanced warming over the global subtropical western boundary currents. *Nature Climate Change* **2**, 161–166 (2012).
32. Argo. Argo float data and metadata from Global Data Assembly Centre (Argo GDAC). SEA-NOE, DOI: 10.17882/42182, <http://doi.org/10.17882/42182> (2019).
33. Good, S. A., Martin, M. J. & Rayner, N. A. EN4: Quality controlled ocean temperature and salinity profiles and monthly objective analyses with uncertainty estimates. *Journal of Geophysical Research: Oceans* **118**, 6704–6716 (2013).
34. Balmaseda, M. A., Mogenssen, K. & Weaver, A. T. Evaluation of the ECMWF ocean reanalysis system ORAS4. *Quarterly Journal of the Royal Meteorological Society* **139**, 1132–1161 (2013).

35. Taylor, B. A. H. & Stephens, J. A. The North Atlantic Oscillation and the latitude of the Gulf Stream. *Tellus* **50A**, 134–142 (1998).
36. Häkkinen, S. & Rhines, P. B. Decline of Subpolar North Atlantic Circulation During the 1990s. *Science* **304**, 555–560 (2004).
37. Caesar, L., Rahmstorf, S., Robinson, A. & Feulner, G. Observed fingerprint of a weakening Atlantic Ocean overturning circulation. *Nature* **556**, 191–196 (2018).
38. Thornalley, D. J. R. *et al.* Atlantic overturning during the past 150 years. *Nature* **556**, 227–230 (2018).
39. Seidov, D., Mishonov, A., Reagan, J. & Parsons, R. Eddy-Resolving In Situ Ocean Climatologies of Temperature and Salinity in the Northwest Atlantic Ocean. *Journal of Geophysical Research: Oceans* **124**, 41–58 (2019).
40. Seidov, D., Mishonov, A., Reagan, J. & Parsons, R. Multidecadal variability and climate shift in the North Atlantic Ocean. *Geophysical Research Letters* **44**, 4985–4993 (2017).
41. Maze, G., Forget, G., Buckley, M., Marshall, J. & Cerovecki, I. Using Transformation and Formation Maps to Study the Role of Air – Sea Heat Fluxes in North Atlantic Eighteen Degree Water Formation. *Journal of Physical Oceanography* **39**, 1818–1835 (2009).
42. Xu, X., Rhines, P. B. & Chassignet, E. P. On Mapping the Diapycnal Water Mass Transformation of the Upper North Atlantic Ocean. *Journal of Physical Oceanography* **48**, 2233–2258 (2018).

43. Schlunegger, S. *et al.* Emergence of anthropogenic signals in the ocean carbon cycle. *Nature Climate Change* **9**, 719–725 (2019).
44. Capotondi, A., Alexander, M. A., Bond, N. A., Curchitser, E. N. & Scott, J. D. Enhanced upper ocean stratification with climate change in the CMIP3 models. *Journal of Geophysical Research* **117**, 1–23 (2012).
45. Hazeleger, W. & Drijfhout, S. S. Mode Water Variability in a Model of the Subtropical Gyre: Response to Anomalous Forcing. *Journal of Physical Oceanography* **28**, 266–288 (1998).

Methods

BATS and Hydrostation S data. The BATS and Hydrostation S measurements can be separated into two distinct datasets: bottle data and CTD data. Since October 1988, CTD sampling has occurred at the BATS and Hydrostation S sites on a monthly and twice-monthly basis, respectively. The data used are fully processed hydrographic profiles that have been subject to calibration and quality control routines prior to release. Information regarding CTD processing and QC procedures are detailed at http://bats.bios.edu/wp-content/uploads/2017/07/report_methods.pdf. In our analysis, CTD profiles shallower than 490 m were discarded, ensuring that the upper and lower boundaries of the STMW layer could be defined.

The bottle data used in this study consist of discrete water samples of hydrographic properties (i.e. temperature and salinity) from the Hydrostation S site spanning February 1955 –September 1988. The vertical resolution of these samples ranges from 10 to 28 samples in the top 600 m

per cast (a median of 13 samples per cast) with a twice-monthly temporal resolution. There are some gaps in this dataset, most markedly for the 15 month period between January 1979 and April 1980, during which no profiles are available. Any profiles with less than 10 samples in the 0–600 m range were discarded, and any profiles with 10–12 samples were linearly interpolated onto the depth resolution of the regular sampling regime (12 depths between 0–600 m). To create a comparable dataset to the primary BATS/Hydrostation S CTD dataset, the physical properties from the water samples (temperature, salinity, and pressure) were interpolated onto a similar depth grid to that of the CTD data using a linear scheme. Then, the datasets were combined and subjected to identical analyses as described in the previous section. The results from these analyses were subsequently window averaged into annual mean values. A total of 5,402 hydrographic profiles were selected from the BATS and Hydrostation S datasets for analysis.

Additional datasets. Our study uses two reanalysis products to assess STMW variability: (1) EN4g10—the fourth version of the Met Office Hadley Centre “EN” series of objective analyses data—is an optimally interpolated dataset produced from a large archive of hydrographic measurements, providing temperature and salinity objective analyses estimates on a $1^\circ \times 1^\circ$ horizontal grid with 42 vertical levels and monthly temporal resolution³³; and (2) ORAS4 —an ECMWF product derived from data assimilation within an ocean global circulation model that produces temperature and salinity estimates on a $1^\circ \times 1^\circ$ horizontal grid with 42 vertical levels and monthly temporal resolution³⁴. The datasets were constrained between $77\text{--}43^\circ\text{W}$, $28\text{--}42^\circ\text{N}$, from January 1955 to July 2019 (EN4g10) and January 1958 to December 2017 (ORAS4), inclusive. To calculate STMW properties at the Bermuda sites (Figure 4), monthly profiles from the nearest grid cells

were used. To calculate the spatial distribution of STMW from the formation zone (Figure 5), profiles at each grid cell were averaged into three-monthly means (e.g. January–March, April–June etc.) prior to STMW calculations for computational ease. For the BV comparisons in Figure 5b–i, the data were spatially interpolated to the BV station locations using a linear interpolation method. Detailed explanations of each dataset are given in the references provided.

In addition to the Bermuda time-series’ and reanalysis products, we also use observations from the Argo program to assess STMW variability throughout the subtropical gyre³². Hydrographic profiles (temperature and salinity) from all floats profiling within 75–45 °W, 30–41°N at any time during the program were downloaded from the CORIOLIS Data Center. Any profiles shallower than 600m deep were discarded. The number of profiles in this region totalled 7,563 ranging from December 2002–September 2019 (see Extended Data Figure 3 for a map detailing the Argo profile locations).

Classification of STMW layer properties. The PV profile from the upper ocean has long been used to define the location of the STMW layer due to the characteristic PV minima produced by the near-homogenous density of STMW^{5,16,21}. The PV profiles were calculated:

$$Q = \frac{f}{\sigma_\theta} \frac{\partial \sigma_\theta}{\partial z} \quad (1)$$

where f is the Coriolis parameter, z is the depth, and σ_θ is the potential density. The contribution of relative vorticity to the PV is assumed to be negligible²⁸. The PV profiles were smoothed before analysis using a 35-point moving window average.

The STMW properties were derived using several different methods. To classify the thickness of the STMW layer, we implemented a two-criteria identification method based on common STMW identification methods¹⁵: the layer must be between the 17 °C and 19 °C isotherms, and the potential vorticity must be $< 1 \times 10^{-10} \text{ m}^{-1} \text{ s}^{-1}$. Imposing the PV criterion reduces the thickness by 26%. While this is a conventional method to identify STMW within a hydrographic profile, there are other methods that use different criteria to demarcate the STMW layer. A discussion on these methods and their impact on the STMW signals presented here is provided in the Supplementary Information, Extended Data Figure 4, and Extended Data Figure 5.

The STMW intensity, I , is a measure of the integrated PV anomaly within the 17 °C and 19 °C isotherms^{1,2}, quantifying the strength of the STMW layer as a function of both its thickness and PV content:

$$I = \int_{z_2}^{z_1} (Q_0 - Q) dz \quad (2)$$

where z_2 is the depth of the 17 °C isotherm, z_1 is the depth of the 19 °C isotherm, and Q_0 is an STMW threshold of $2 \times 10^{-10} \text{ m}^{-1} \text{ s}^{-1}$, and $Q < Q_0$. Initially, in line with previous North Atlantic studies¹, a value of $1 \times 10^{-10} \text{ m}^{-1} \text{ s}^{-1}$ was applied as the STMW threshold. We found, however, that $Q > Q_0$ during weak formation periods. To account for this, we increased the threshold value to $2 \times 10^{-10} \text{ m}^{-1} \text{ s}^{-1}$, as implemented in the higher PV waters of the North Pacific². One drawback of using this method is that the threshold value Q_0 is much larger than the PV within the layer, therefore the variance of the data is very small. This makes comparisons between the

two periods of weak intensity less effective, resulting in similar values of STMW intensity with overlapping confidence limits (Extended Data Figure 2). Thus, while STMW intensity is a good measure of the variability in the STMW signal, it is not necessarily a good metric for statistical comparison in this context.

Here, the STMW core is defined as the PV minimum found between 16 °C and 20 °C isotherms. A slightly less stringent isotherm range was used here as a small amount of profiles had STMW cores located outside of the 17–19 °C isotherms due to: (1) considerable mesoscale variability; and (2) anomalously warm STMW layers occurring later in the time-series. Considering this, 82% of the STMW cores derived in this manner had a temperature between 17–19 °C, and >99% had a PV of $<1 \times 10^{-10} \text{ m}^{-1} \text{ s}^{-1}$. The desired physical properties in the STMW core (i.e. temperature) were interpolated to the core depth level using a linear interpolation scheme.

Specific enthalpy is an effective measure of the heat content of seawater³. It is calculated here as a vertical integral:

$$h = \int_{z_L}^{z_U} \left(g - T \frac{\partial g}{\partial T} |_{\mathbf{S}, \mathbf{P}} \right) dz \quad (3)$$

where z_U is 10 m for h_s or the upper STMW boundary for h_{STMW} , z_L is 150 m for h_s or the lower STMW boundary for h_{STMW} , g is the exact Gibbs function, T is the in-situ temperature, S is the absolute salinity, and P is the pressure. Further information on specific enthalpy can be found in the TEOS-10 manual³.

All datasets were subject to identical analytical techniques to derive STMW properties.

Formation zone analyses. To define the STMW formation zone, we took subsets of the EN4g10 and ORAS4 reanalysis data from 75–45 °W, 30–41°N (study regions are detailed in Figure 1a). These data subsets enclose the primary formation zone⁴¹, however the northern edges of our subsets extend further north to capture the northernmost extent of the 17 °C SST contour during the observation period. To evaluate the wintertime STMW formation, the formation zone hydrography was temporally averaged between February and April (inclusive, the STMW formation season^{1,17}) for the period 1955 to 2018, producing mean wintertime depth profiles of physical parameters for each year. Profiles that were found to have outcropping isotherms of 17–19 °C were used to calculate the annual STMW outcropping volume, V_f :

$$V_f = \sum x_i y_i z_i \quad (4)$$

where x is the zonal distance between grid points, y is the meridional distance between grid points, and z is the STMW thickness (i.e. the depth of the 17 °C isotherm), with the summation occurring over all outcropping grid cells.

Analyses were performed on every reanalysis grid cell in an identical manner to the BATS/Hydrostation S dataset to classify the STMW layer, as well as to calculate h_s and other properties.

BATS Validation dataset. The BV dataset is an extension of the BATS dataset, where a meridional transect of CTD stations with one-degree spacing is performed annually from 34–20°N along

the 66.5°W meridian. The CTD sampling at these stations is identical to that at BATS. Stations with less than 10 CTD profiles were deemed to be insufficiently sampled for analysis and were discarded. The remaining stations were annual time-series of 10–18 years. These stations were subject to the same analysis as the BATS and extended Hydrostation S datasets. It should be noted that one component of the BV transect is a station at the BATS site, indicated on Figure 5 as a green marker at the same along-transect distance as the BATS site. This BV data is independent of the BATS/Hydrostation S dataset.

NAO Index. To assess the impact of NAO forcing upon STMW properties, we use the station-based NAO DJFM index. This index represents the mean NAO values from December (year n-1) to March (year n; for example, the 2017 DJFM index will be the mean NAO index from December 2016 and January –March 2017). As this index spans the yearly formation period, it has been found to better represent the effect of NAO forcing on STMW renewal²⁰. See Extended Data Figure 4 for information on NAO-STMW relationship in this study.

Statistics. All trends in our study were calculated using a Theil-Sen estimator—a robust, non-parametric method for fitting a linear regression to heteroskedastic data⁴. All trends are statistically significant at a level of 0.05 or below unless otherwise stated. The significance was assessed using a non-parametric, two-tailed Mann-Kendall test⁵. Property trends in the BATS/Hydrostation S analysis (i.e. Table 1 and any references to these values in the body of the text, and Figure 2), were calculated using the full resolution dataset, not the annual means. To assess trend uncertainty, the standard deviation around the regression was calculated:

$$U = \sqrt{\frac{\sum(y_o - y_t)^2}{n - 2}} \quad (5)$$

where y_o are the observed data points, y_t are the values derived from the regression, and n is the number of observations. Subsequently, the trend uncertainty is calculated:

$$U_{y/x} = \frac{2U}{\sqrt{\sum(x_i - \bar{x})^2}} \quad (6)$$

where $2U$ is twice the standard deviation around the regression (representing the 95% confidence interval), x_i are the temporal points from the observations, and \bar{x} is the mean of those points. Property changes over multiple years are calculated as an interval:

$$[P_l, P_u] = T_r(\beta \pm U_{y/x}) \quad (7)$$

Where T_r is the duration of the time range in question and β is the property slope derived from the Theil-Sen estimator.

The 95% confidence intervals for all mean values were calculated as follows:

$$CI = \bar{x}(\pm t)\sigma_{\bar{x}} \quad (8)$$

where \bar{x} is the annual mean of the data, t are the t-scores of the annual dataset, and $\sigma_{\bar{x}}$ is the standard mean error of the dataset. The t-scores were calculated to represent 95% significance

using a Student's t inverse cumulative distribution function with n-1 degrees of freedom. This calculation applies to the annual mean values and confidence limits in Figure 2, the mean values and confidence limits for selected periods in Table 1 and any other mean values stated within the manuscript

Time-series plotting. Annual values were plotted centrally for their corresponding year (i.e. annual values for 1993 are plotted at x=1993 etc.).

Data availability. The authors declare that all data supporting the findings of this study can be found in the following online repositories: the BATS CTD data can be found at <http://batsftp.bios.edu/BATS/> and the Hydrostation S CTD and extended bottle datasets are available at http://batsftp.bios.edu/Hydrostation_S/. The ECMWF ORAS4 dataset can be accessed at <https://climatedataguide.ucar.edu/climate-data/oras4-ecmwf-ocean-reanalysis-and-derived-ocean-heat-content>. The Met Office Hadley Centre EN4g10 dataset can be accessed at <https://www.metoffice.gov.uk/hadobs/en4/download-en4-2-0.html>. The NAO index (DJFM) data can be accessed at <https://climatedataguide.ucar.edu/climate-data/hurrell-north-atlantic-oscillation-nao-index-station-based>. The Argo data can be accessed at <https://doi.org/10.17882/42182>. The final Argo data used in this study was accessed on 10th October 2019.

Code availability. All custom code used in this study can be found at <https://doi.org/10.5281/zenodo.3620816>.

1. Billheimer, S. & Talley, L. D. Annual cycle and destruction of Eighteen Degree Water. *Journal of Geophysical Research: Oceans* **121**, 6604–6617 (2016).

2. Qiu, B., Chen, S. & Hacker, P. Effect of Mesoscale Eddies on Subtropical Mode Water Variability from the Kuroshio Extension System Study (KESS). *Journal of Physical Oceanography* **37**, 982–1000 (2006).
3. IOC, S. & IAPSO. The international thermodynamic equation of seawater – 2010: Calculation and use of thermodynamic properties, Intergovernmental Oceanographic Commission, Manuals and Guides No. 56, UNESCO (English) (2010).
4. Sen, P. K. Estimates of the Regression Coefficient Based on Kendall’s Tau. *Journal of the American Statistical Association* **63**, 1379–1389 (1968).
5. Kendall, A. M. G. A New Measure of Rank Correlation. *Biometrika* **30**, 81–93 (1938).

Author contributions N.R.B. and R.J.J. are principal investigators for the BATS/Hydrostation S projects and coordinate the sampling and analysis of data. S.W.S., N.R.B., and R.J.J. designed the study and composed the BATS/Hydrostation S analyses. S.W.S. and G.M. investigated the reanalysis datasets. S.W.S. wrote the manuscript with contributions from N.R.B., R.J.J., and G.M..

Competing financial interests The authors declare no competing interests.

Correspondence Correspondence and requests for materials should be addressed to S.W.S. (sstevens@eoas.ubc.ca).

Acknowledgements The authors would like to acknowledge and thank the numerous principal investigators, researchers, and technicians who have contributed to the time-series projects since their inception. Additional thanks go to the officers and crew of the R/V *Weatherbird I*, R/V *Weatherbird II* and R/V *Atlantic*

Explorer. This work was funded by NSF grant OCE-1633215 and supported by the French national program LEFE/INSU project SOMOVAR “North-Atlantic Subtropical Ocean: Mechanisms of Observed and projected low-frequency variability”.

Parameter	Period	Mean (95% C.L.)	Change over period	Slope (per year) $\pm 2 \sigma_{\bar{x}}$	n	r^2	p -value
Thickness	1967–1975	201 (187–215) m	-216 – -125 m	-18.9 \pm 5.0	132	0.30	<0.01
Intensity	1967–1975	2.8 (2.5–3.0) $\times 10^{-8} \text{ s}^{-1}$	-2.9 – -1.3 $\times 10^{-8} \text{ s}^{-1}$	-0.24 \pm 0.09 $\times 10^{-8} \text{ s}^{-1}$	132	0.21	<0.01
Core PV	1967–1975	4.0 (3.6–4.4) $\times 10^{-11} \text{ m}^{-1} \text{ s}^{-1}$	4.0 – 6.4 $\times 10^{-11} \text{ m}^{-1} \text{ s}^{-1}$	0.58 \pm 0.14 $\times 10^{-11} \text{ m}^{-1} \text{ s}^{-1}$	112	0.34	<0.01
Thickness	2010–2018	174 (170–179) m	-280 – -260 m	-30.0 \pm 1.2 m	2218	0.56	<0.01
Intensity	2010–2018	2.9 (2.8–2.9) $\times 10^{-8} \text{ s}^{-1}$	-2.9 – -2.6 $\times 10^{-8} \text{ s}^{-1}$	-0.30 \pm 0.02 $\times 10^{-8} \text{ s}^{-1}$	2218	0.47	<0.01
Core PV	2010–2018	5.3 (5.2–5.4) $\times 10^{-11} \text{ m}^{-1} \text{ s}^{-1}$	4.6 – 5.5 $\times 10^{-11} \text{ m}^{-1} \text{ s}^{-1}$	0.54 \pm 0.04 $\times 10^{-11} \text{ m}^{-1} \text{ s}^{-1}$	2096	0.21	<0.01
Thickness	1955–2013	253 (250–255) m	-17 – -3 m	<1 m	3864	0.00	0.12
Intensity	1955–2013	3.8 (3.8–3.9) $\times 10^{-8} \text{ s}^{-1}$	0.03 – 0.38 $\times 10^{-8} \text{ s}^{-1}$	<0.01 $\times 10^{-8} \text{ s}^{-1}$	3864	0.00	0.02
Core PV	1955–2013	3.7 (3.6–3.7) $\times 10^{-11} \text{ m}^{-1} \text{ s}^{-1}$	<0.1 $\times 10^{-11} \text{ m}^{-1} \text{ s}^{-1}$	<0.01 $\times 10^{-11} \text{ m}^{-1} \text{ s}^{-1}$	3654	0.00	0.43
Thickness	1955–2019	219 (217–222) m	-269 – -246 m	-4.1 \pm 0.2 m	5402	0.10	<0.01
Intensity	1955–2019	3.4 (3.3–3.4) $\times 10^{-8} \text{ s}^{-1}$	-3.6 – -3.2 $\times 10^{-8} \text{ s}^{-1}$	-0.05 \pm <0.01 $\times 10^{-8} \text{ s}^{-1}$	5402	0.06	<0.01
Core PV	1955–2019	4.4 (4.3–4.4) $\times 10^{-11} \text{ m}^{-1} \text{ s}^{-1}$	4.8 – 5.3 $\times 10^{-11} \text{ m}^{-1} \text{ s}^{-1}$	0.08 \pm <0.01 $\times 10^{-11} \text{ m}^{-1} \text{ s}^{-1}$	5085	0.09	<0.01

Table 1: Statistics of STMW parameters over various time periods of interest. All date ranges are inclusive. These time periods span the two periods of substantial STMW decline (1966–1974 and 2010–2018), as well as the 1955–2013 period and the dataset in its entirety (February 1955–September 2019). Period means are expressed with 95% confidence limits calculated as the product of $\sigma_{\bar{x}}$ and the sample t-scores. Change over period is calculated as the slope per year \pm the error estimates multiplied by the length of the period (in years). Slopes are calculated using a Sen-Theil estimator $\pm 2\sigma_{\bar{x}}$ of the slope. Property change over a period is calculated as the product of the time range duration and the uncertainty limits of the slope. See methods section for further information on statistics.

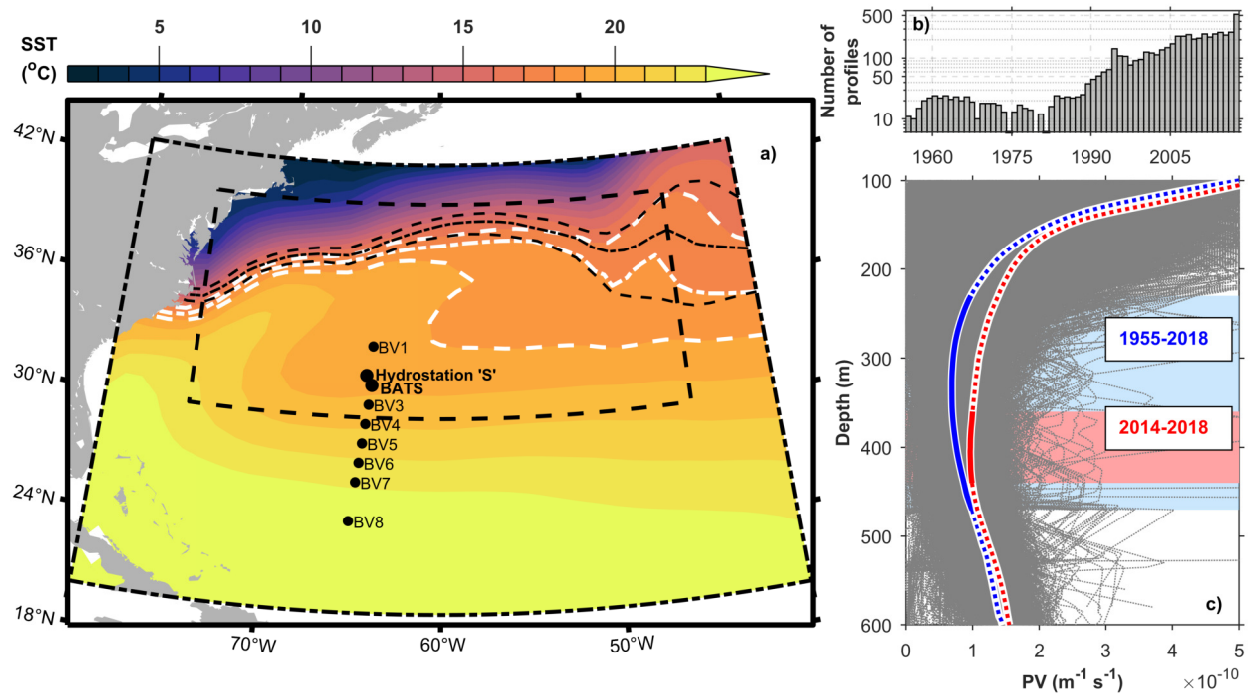


Figure 1: A map of the study zone and hydrographic profile information. In a) the black dot-dash rectangle denotes the outer limits of the Met Office Hadley Centre EN4g10 dataset. The black dash rectangle represents the outer limits of the formation zone used in our study, and the filled contour map denotes the mean SST for the winter (February–April, inclusive) formation period from 1955–2019. The white dashed contours denote the mean STMW outcropping region (17 °C and 19 °C contours), and the white dot-dash contour represents the mean core position of the formation zone (18 °C contour) from 1955–2019. The black contours denote the same outcropping zones from 2014–2018. The black scatter points denote the locations of BATS, Hydrostation S, and BATS Validation stations. b) A histogram of the number of physical profiles per year used in our study from February 1955–September 2019 (5402 total) and c) smoothed PV depth profiles. The grey dotted lines denote the individual profiles from the study, the coloured line denotes the mean PV depth profile from two different periods: 1955-2018 (blue) and 2014-2018 (red). The solid section of the lines indicate where the PV is less than $1 \times 10^{-10} \text{ m}^{-1} \text{ s}^{-1}$, identifying it as STMW.

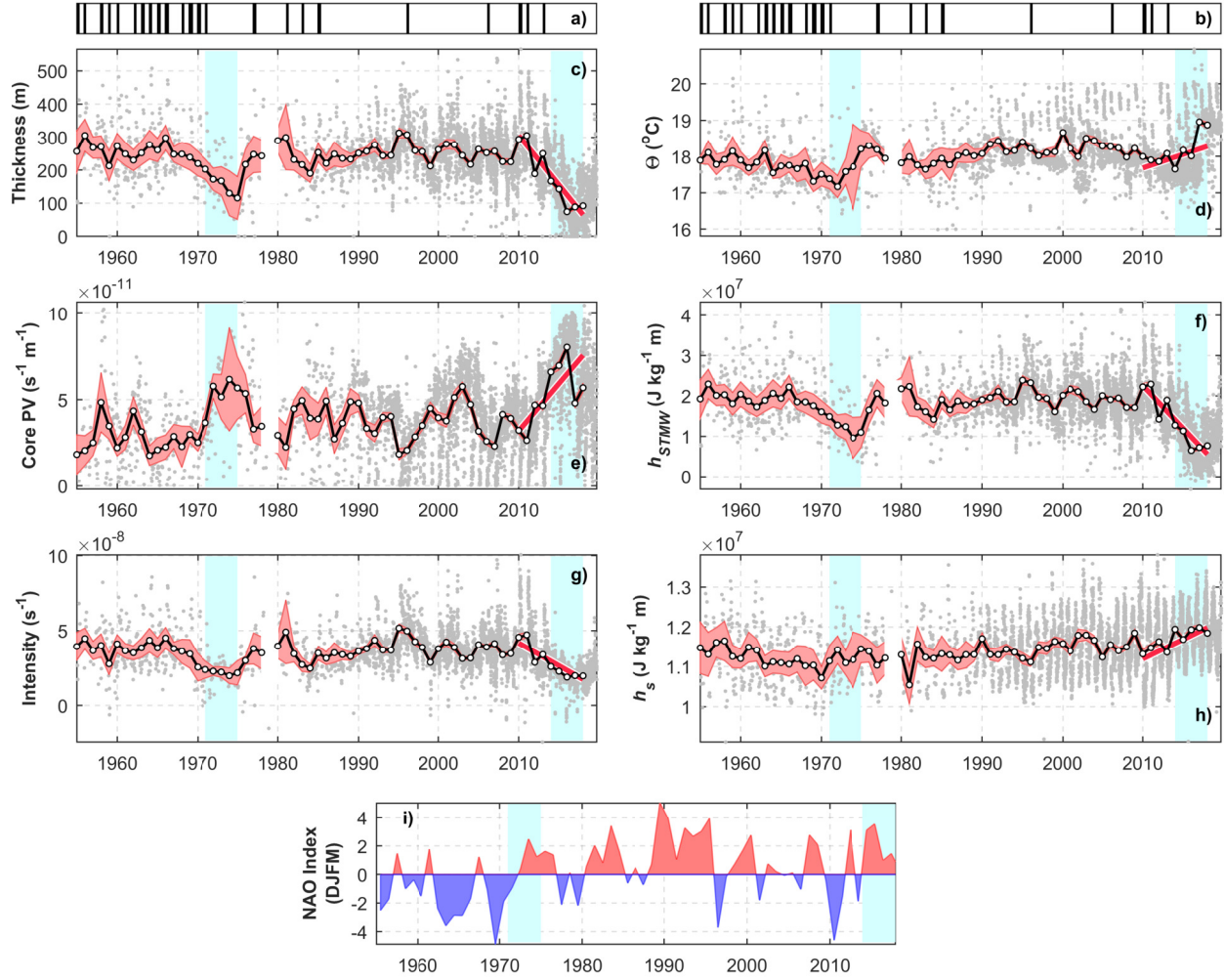


Figure 2: Time-series plots of STMW properties from February 1955–September 2019. Vertical lines in a) and b) denote periods where $<19^{\circ}\text{C}$ outcropping occurred at BATS/Hydrostation S. Variations in STMW: (c) thickness; (d) core temperature; (e) core PV; (f) h_{STMW} ; (g) intensity; and, (h) h_s . Grey scatter points represent all observations, solid black lines with white markers denote annual mean values (1955–2018), solid red lines denote 2010–2018 trends, and red shading represents the 95% confidence limits of the annual means. NAO index (DJFM) is plotted for the same period (i; red shading denotes NAO positive periods and blue shading denotes NAO negative periods). Weak STMW pentads (1971 to 1975 and 2014 to 2018) are indicated by cyan boxes in all plots. Annual means are expressed with 95% confidence limits calculated as the product of $\sigma_{\bar{x}}$ multiplied by the sample t-scores. Slopes are calculated using a Sen-Theil estimator $\pm 2\sigma_{\bar{x}}$ of the slope. See methods section for further information on statistics.

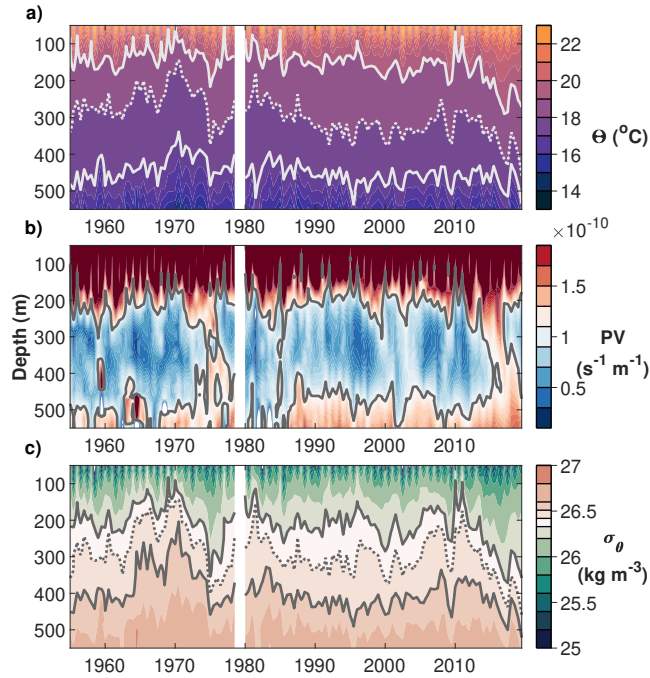


Figure 3: Six-month window averaged conditions from BATS and Hydrostation S. Contour plots of (a) temperature; (b) PV; and c) σ_θ from the upper ocean. Solid white/grey contours indicate boundaries of the SMTW layer: (a) the 17 °C and 19 °C isotherms; (b) the $1 \times 10^{-10} \text{ m}^{-1} \text{ s}^{-1}$ PV contour; and (c) the 26.3 kg m^{-3} and 26.5 kg m^{-3} isopycnals. In a) and c), the STMW core is denoted by the dotted contours: a) 18 °C isotherm and c) 26.4 kg m^{-3} isopycnal.

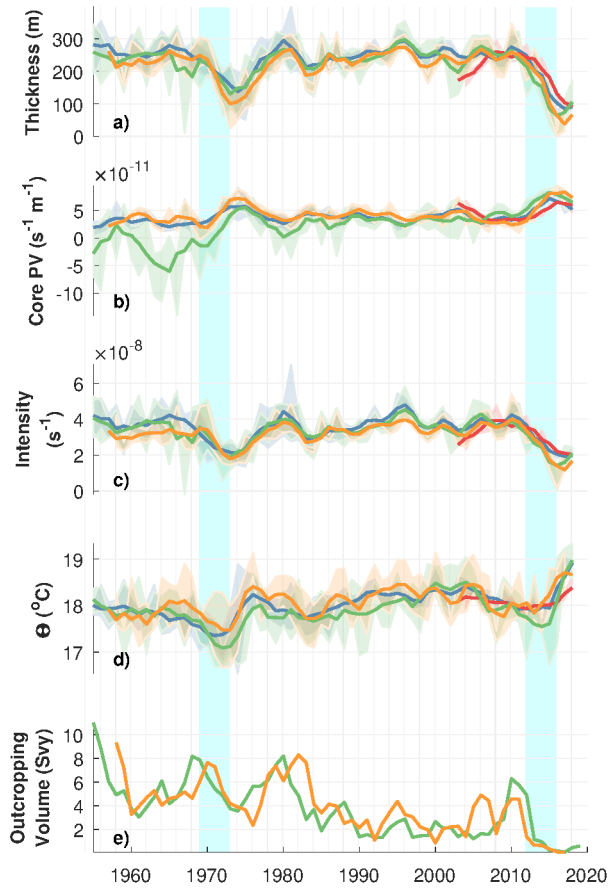


Figure 4: Time-series plots of STMW properties from observational and reanalysis datasets. a) thickness; b) core PV; c) intensity; d) core temperature; and e) outcropping volume. Blue lines denote BATS/Hydrostation S data, red lines denote Argo float data, green lines denote EN4g10 data, and yellow lines denote ORAS4 data. Signals were averaged into annual means and smoothed with 3 year moving-mean. Shading represents 95% confidence limits for the annual means. Argo float hydrographic profiles were extracted from the STMW formation zone between 2002 and 2018, totaling 7,563 profiles. Reanalysis data were taken from the grid points closest to the BATS site between 1955 and 2018. Cyan shading represent weak mode formation periods. The 95% confidence limits calculated as the product of $\sigma_{\bar{x}}$ multiplied by the sample t-scores. See methods section for further information on statistics.

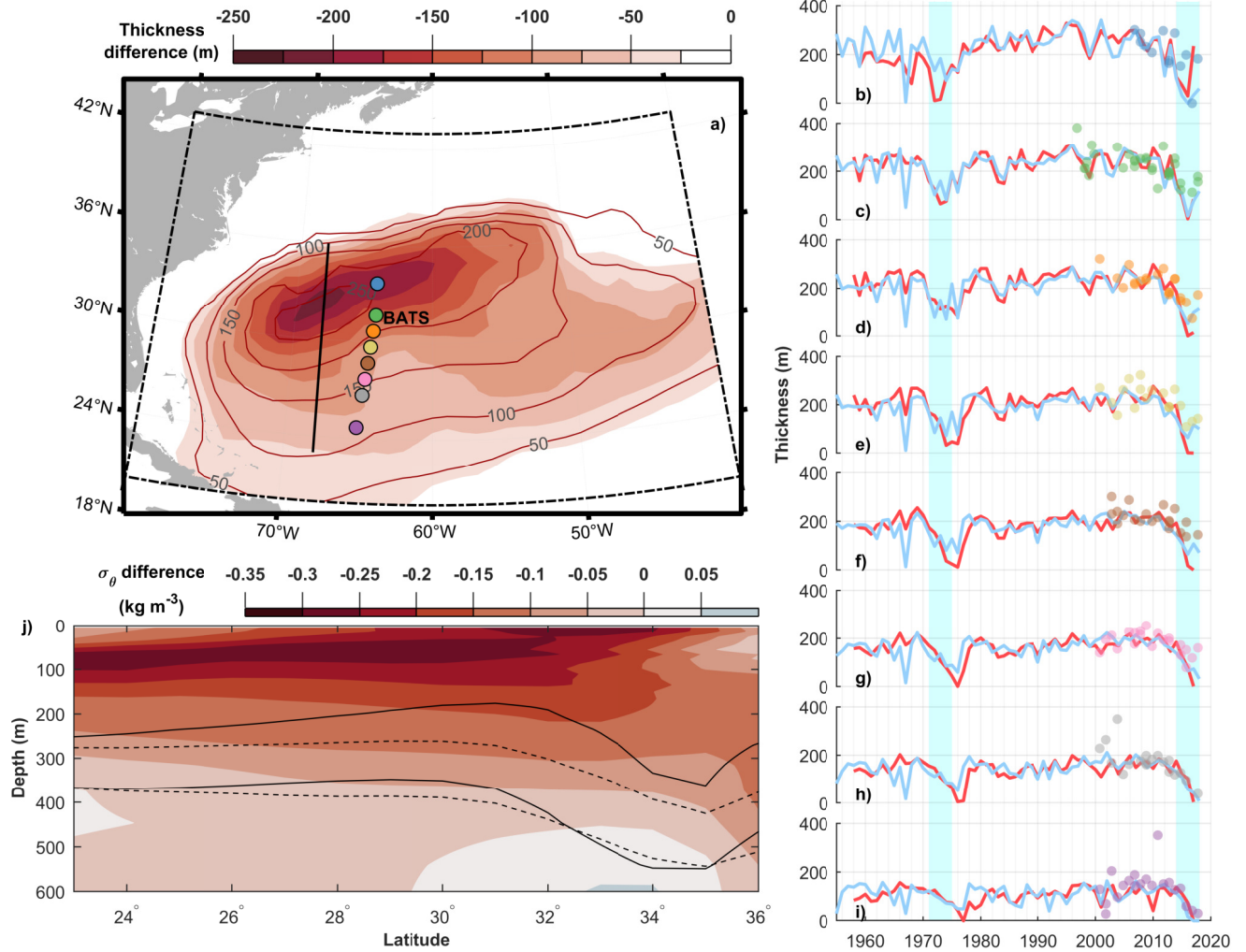


Figure 5: Spatiotemporal variability of STMW thickness in the North Atlantic subtropical gyre. Difference map a) denotes the STMW thickness difference between 2014–2018 and 1955–2013 (inclusive; derived from the EN4g10 dataset; negative values indicate STMW loss in 2014–2018). Overlaid contour lines show mean STMW thickness prior to 2014. Black dot-dash line encloses model region. Straight black line denotes 68°W meridional transect. BATS Validation stations are depicted by coloured points. Thickness time-series b)-i) show EN4g10 (blue) and ORAS4 (red) data spatially interpolated to the BATS Validation stations using a linear interpolation scheme, with the BATS Validation data scattered on top (colors correspond to station colors on the map). Contour plot j) depicts the density change along the 68°W meridional transect. Density (σ_θ) difference compares the 2010–2019 density to the density preceding 2010 (negative values denote decreased densities during the 2010–2019 period). Black contours show the depth of the 26.3 kg m^{-3} and 26.5 kg m^{-3} contours from before 2014 (solid black lines) and after 2014 (dashed black lines).

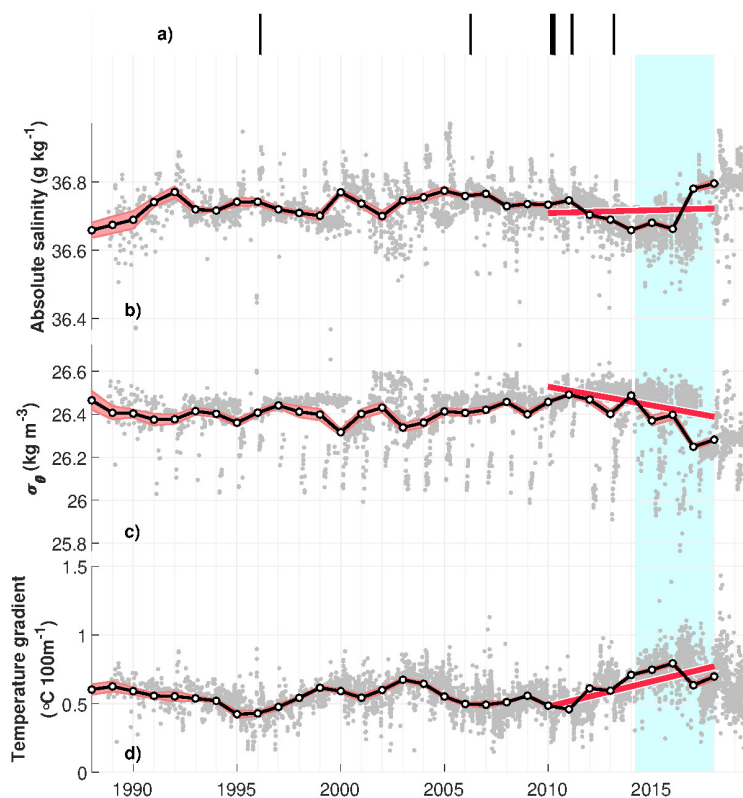


Figure ED1: Time-series plots of STMW core properties. Time-series of (a) $<19^{\circ}\text{C}$ surface outcropping denoted by black vertical lines; (b) absolute salinity; (c) potential density anomaly; and (d) temperature gradient per 100 m from January 1988 to September 2019. Temperature gradient was calculated as the maximum temperature gradient, per metre, found in the identified STMW layer, multiplied by 100. Grey scatter points represent the full resolution time-series, solid black lines with white markers represent annual means, red shading represents the 95% confidence limits of the annual means, and red lines represent 2010-2018 trends (p -values <0.05). Weak STMW pentad (2014-2018) is indicated by a cyan box. Annual means are expressed with 95% confidence limits calculated as the product of $\sigma_{\bar{x}}$ multiplied by the sample t -scores. Slopes are calculated using a Sen-Theil estimator $\pm 2 \sigma_{\bar{x}}$ of the slope. See methods section for further information on statistics.

Dataset	Period	Thickness (m)	Intensity (s ⁻¹)	Core PV (m ⁻¹ s ⁻¹)	n
BATS/Hydrostation S	1971-1975	146-184	2.0-2.5 x 10 ⁻⁸	4.6-5.6 x 10 ⁻¹¹	67
	2014-2018	109-116	2.1-2.2 x 10 ⁻⁸	6.3-6.5 x 10 ⁻¹¹	1289
Argo	2014-2018	154-161	2.5-2.6 x 10 ⁻⁸	5.6-5.8 x 10 ⁻¹¹	3642
EN4g10	1971-1975	131-182	1.8-2.5 x 10 ⁻⁸	2.4-4.5 x 10 ⁻¹¹	60
	2014-2018	72-113	1.5-2.5 x 10 ⁻⁸	6.9-7.8 x 10 ⁻¹¹	60
ORAS4	1971-1975	106-148	1.9-2.3 x 10 ⁻⁸	5.5-6.7 x 10 ⁻¹¹	60
	2014-2017	68-118	1.4-2.0 x 10 ⁻⁸	7.3-8.1 x 10 ⁻¹¹	48

Figure ED2: Statistical comparison of STMW parameters for the two weakest STMW periods. All date ranges are inclusive. The Argo and ORAS4 datasets are incomplete for certain periods. Ranges are expressed as the 95% confidence intervals of the mean properties within a given period, calculated as the product of σ_x and the sample t-scores. See methods section for further information on statistics.

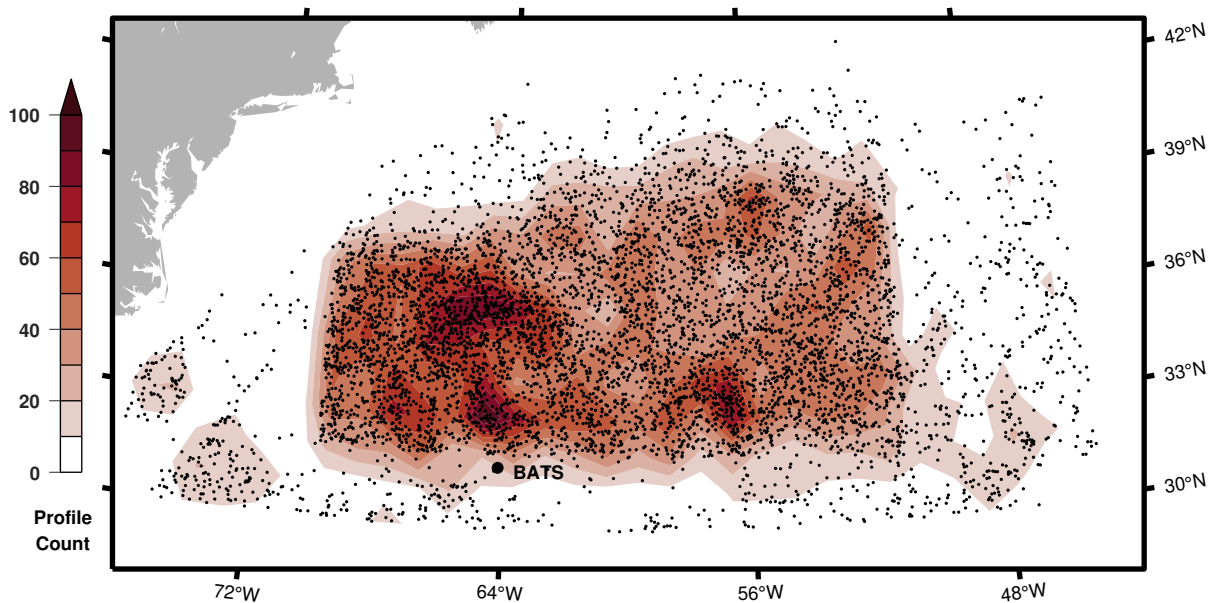


Figure ED3: Map of Argo float profiles. Heat map denotes the amount of Argo profiles performed in 1° x 1° grid cells within the formation zone. Scattered points denote the locations of individual profiles in within the formation zone.

Definition	Temperature threshold	PV threshold	Other
Less Stringent (LS)	16 – 20°C	$< 2 \times 10^{-10} \text{ s}^{-1} \text{ m}^{-1}$	-
More Stringent (MS)	17.5 – 18.5°C	$< 1 \times 10^{-10} \text{ s}^{-1} \text{ m}^{-1}$	-
Density only (DO)	-	-	26.3-26.5 σ_θ
Density included (DI)	17 – 19°C	$< 1 \times 10^{-10} \text{ s}^{-1} \text{ m}^{-1}$	26.3-26.5 σ_θ
Billheimer and Talley, 2016 (BT)	17 – 19°C	-	26.2-26.7 σ_θ
BATS/Hydrostation S (BH)	17 – 19°C	$< 1 \times 10^{-10} \text{ s}^{-1} \text{ m}^{-1}$	$< 0.006^\circ \text{C m}^{-1}$

Figure ED4: Table detailing different STMW definitions. Different STMW definitions and associated physical classifications employed in Extended Data Figure 5.

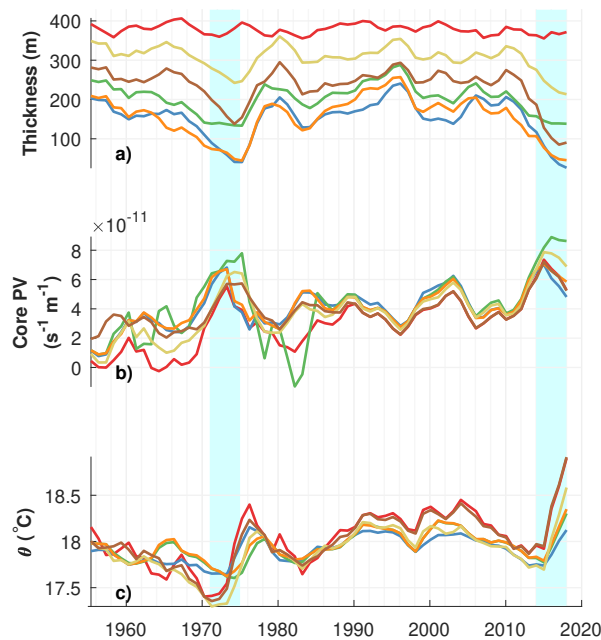


Figure ED5: Time-series plots of STMW properties based on different identification algorithms. Data were averaged into annual means and the resulting signal was smoothed using a three-year moving mean. Red lines represent LS definition, blue lines represent MS definition, green lines represent DO definition, orange lines represent DI definition, olive lines represent BT definition, and brown lines represent BH definition. See Extended Data Figure 4 for details of STMW definitions. Annual means are expressed with 95% confidence limits calculated as the product of $\sigma_{\bar{x}}$ multiplied by the sample t-scores. See methods section for further information on statistics.

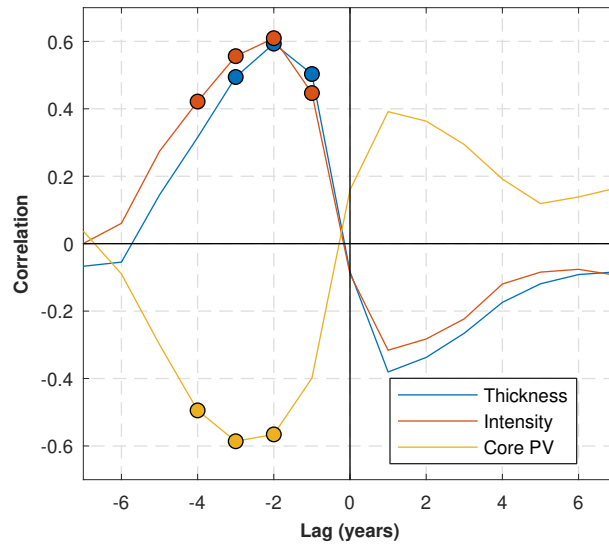


Figure ED6: NAO-STMW correlation time-series. Lag correlation plot for three-year centred moving average of the NAO DJFM index and the three primary measures of STMW strength. Negative lag occurs when NAO DJFM index leads STMW properties, positive lag occurs when NAO DJFM index lags STMW properties. Filled markers denote lags at which correlations are significant with p -values < 0.05 .